



Swansea University
Prifysgol Abertawe



Cronfa - Swansea University Open Access Repository

This is an author produced version of a paper published in:

Computational Mechanics

Cronfa URL for this paper:

<http://cronfa.swan.ac.uk/Record/cronfa13205>

Paper:

Xie, Z., Sevilla, R., Hassan, O. & Morgan, K. (in press). The generation of arbitrary order curved meshes for 3D finite element analysis. *Computational Mechanics*, 51(3), 361-374.

<http://dx.doi.org/10.1007/s00466-012-0736-4>

This item is brought to you by Swansea University. Any person downloading material is agreeing to abide by the terms of the repository licence. Copies of full text items may be used or reproduced in any format or medium, without prior permission for personal research or study, educational or non-commercial purposes only. The copyright for any work remains with the original author unless otherwise specified. The full-text must not be sold in any format or medium without the formal permission of the copyright holder.

Permission for multiple reproductions should be obtained from the original author.

Authors are personally responsible for adhering to copyright and publisher restrictions when uploading content to the repository.

<http://www.swansea.ac.uk/iss/researchsupport/cronfa-support/>

The generation of arbitrary order curved meshes for 3D finite element analysis

Zhong Q. Xie, Ruben Sevilla, Oubay Hassan, Kenneth Morgan

Abstract

A procedure for generating curved meshes, suitable for high-order finite element analysis, is described. The strategy adopted is based upon curving a generated initial mesh with planar edges and faces by using a linear elasticity analogy. The analogy employs boundary loads that ensure that nodes representing curved boundaries lie on the true surface. Several examples, in both two and three dimensions, illustrate the performance of the proposed approach, with the quality of the generated meshes being analysed in terms of a distortion measure. The examples chosen involve geometries of particular interest to the computational fluid dynamics community, including anisotropic meshes for complex three dimensional configurations.

Keywords: mesh generation, high-order elements, curved finite elements, element distortion, element stretching, computational fluid dynamics

1. Introduction

The last decade has seen an increase in interest in the development of high-order discretisation methods within the finite element community [29, 15, 11, 16]. The advantages that high-order methods bring, in terms of accuracy and efficiency, have been object of intensive study [17, 5] and, as higher order approximations are considered, the effect of an appropriate boundary representation of the domain has been identified as being critical [24, 26, 27]. The use of curved elements becomes mandatory in order to obtain the advantages of using high-order approximations [8, 1, 18, 37, 25] and the lack

Email addresses: Z.Q.Xie@swansea.ac.uk (Zhong Q. Xie),
R.Sevilla@swansea.ac.uk (Ruben Sevilla), O.Hassan@swansea.ac.uk (Oubay Hassan), K.Morgan@swansea.ac.uk (Kenneth Morgan)

of high-order curved mesh generators for complex geometries is recognised to be an obstacle preventing the widespread application of high-order methods [34]. Existing approaches for constructing a curved high-order mesh can be classified into two categories [6]: the so-called direct methods, which build a curved high-order mesh directly from the CAD representation of the geometry, and the *a posteriori* approach, in which the curved mesh is generated by deforming an initial linear mesh. *A posteriori* approaches are generally preferred, as they makes use of mature linear mesh generation technology [36].

In the basic *a posteriori* approach [6, 7], boundary mesh entities are curved using the parametric space of the underlying geometric model. Curving a linear initial mesh will often create low quality or invalid elements, especially in regions of high curvature, and specific strategies for detecting and correcting invalid elements are therefore necessary [6, 7, 28, 19]. Using a quality measure, derived from the Jacobian of an isoparametric transformation to detect invalid elements, mesh operations such as edge and face swapping, edge deletion, internal entity curving and node relocation are used in an attempt to obtain a valid curved mesh. In addition, it may, sometimes, be necessary [6] to perform remeshing in order to completely remove non valid elements. Different strategies have been proposed for alleviating the problem of invalid elements [28]. These include improving the quality of the curved surface mesh, by constructing an optimal nodal set over the curved faces on the boundary, or using a hybrid mesh of prismatic elements near curved boundaries and tetrahedral elements in the rest of the domain, or using a curvature based mesh refinement strategy to reduce the deformation of curved elements and the possibility of generating non valid elements.

An alternative *a posteriori* approach employs a non-linear elasticity model to deform the initial mesh [20]. The initial linear mesh represents the undeformed state and, after prescribing a boundary displacement based upon the curved geometry, a deformed curved high-order mesh corresponding to the equilibrium state is obtained. Mesh moving techniques based on elasticity equations were proposed in [33], with details given in [13], and have a proven track record of robustness. In Jacobian-based stiffening, as shown in [30], the stiffening power can be varied to obtain the desired effect.

A similar technique is proposed in this paper but, in an attempt to improve the efficiency of the process, a linear elastic model is adopted. In addition, specific strategies for the generation of nodal distributions on edges or faces of curved boundaries are proposed, in order to minimise the possible number of non-valid elements and to enhance the overall quality of

the resulting curved mesh. Particular attention is paid to the generation of anisotropic boundary layer meshes, suitable for the efficient simulation of high Reynolds number fluid flow problems. This is a crucial problem that must be overcome, before high-order methods can be routinely applied by the computational fluid dynamics community to the solution of problems of industrial interest. It is worth noting that the methodology proposed in this paper is valid for any element topology, so that hybrid meshes can also be constructed.

The paper is organised as follows. In Section 2, the linear elastic problem and its solution, using high-order continuous finite elements, is briefly outlined. Sections 3 and 4 describe the proposed approach for generating curved high-order meshes in two and three dimensions respectively. The performance of the proposed method is demonstrated in Section 5 and several examples, involving the generation of isotropic and anisotropic meshes in both two and three dimensions, are considered. Finally, Section 6 summarises the main conclusions of the work that has been presented.

2. High-order finite element solution of the linear elastic problem

The proposed *a posteriori* approach will employ a linear elastic model to deform a mesh that has been generated for the geometry of interest.

The equation governing the static deformation of a linear elastic medium, Ω , with closed boundary Γ , is considered in the form

$$\nabla \cdot \boldsymbol{\sigma} = \mathbf{0} \quad \text{in } \Omega \quad (1)$$

The stress tensor $\boldsymbol{\sigma}$ is given by

$$\boldsymbol{\sigma} = \lambda \text{tr}(\boldsymbol{\varepsilon})\mathbf{I} + 2\mu\boldsymbol{\varepsilon} \quad (2)$$

where $\boldsymbol{\varepsilon}$ is the deformation tensor and λ and μ denote the Lamé coefficients for the medium. This constitutive relation is often expressed, alternatively, in terms of Young's modulus E and Poisson's ratio ν for the medium [39, 38].

The solution to equation (1) is sought subject to appropriate boundary conditions. In the current context, these conditions will be an imposed displacement \mathbf{u}_D on the Dirichlet boundary, Γ^D , and an imposed traction, \mathbf{f}_n , on the Neumann boundary Γ^N . Here, $\Gamma = \Gamma^D \cup \Gamma^N$ and $\Gamma^D \cap \Gamma^N = \emptyset$.

The solution is approximated using continuous piecewise polynomials of order p on a reference element e and an isoparametric finite element formulation is employed [38], so that the physical and local coordinates for element

e are related using the mapping

$$\mathbf{x}(\boldsymbol{\xi}) = \sum_{J=1}^{\text{nen}} N_J(\boldsymbol{\xi}) \mathbf{x}_J \quad (3)$$

where \mathbf{x}_J are the coordinates of node J of the element.

To produce an accurate and efficient high-order finite element solver, appropriate nodal distributions for the interpolation [3, 4, 32] and optimal numerical quadratures for the integration [9, 35, 10] are used. On one hand, optimal interpolation points, such as the Fekete points [32], substantially reduce the interpolation error compared to equally-spaced nodal distributions when very high-order approximations are considered, say $p \geq 4$. On the other hand, optimal numerical quadrature enables a reduction in the computational cost involved in evaluating the integrals that appear in the variational formulation.

3. Two dimensional curved mesh generation

The two dimensional problem of generating a curved mesh, of prescribed order p , is considered first. The basic steps involved in the proposed process are illustrated in Figure 1, which shows how a triangular mesh of degree $p = 4$ can be generated in the region surrounding a general two dimensional object. Initially, Figure 1 (a), the region surrounding the object is discretised with linear triangular elements using a standard two dimensional unstructured mesh generator. The characteristic mesh size, h , of this initial mesh is selected in such a way that the characteristic mesh size of the final high-order mesh, h/p , will provide a spatial discretisation that is suitable for resolving the features of interest in the problem under consideration. Nodes, appropriate to the selected degree of approximation, p , are located on each straight-sided element. In Figure 1 (b), the nodes have been located at the Fekete points [32]. Then, for each pair of edge vertices on a curved boundary, the desired location for the nodes on the true boundary is computed, as shown in Figure 1 (c). The process is completed by obtaining a high-order solution to the linear elasticity problem, with the mesh of straight-sided elements forming the initial configuration. With Dirichlet boundary conditions corresponding to the displacement of boundary nodes, from their initial location on straight sides to their desired location on the true boundary, the equilibrium configuration is the curved high-order mesh of Figure 1 (d).

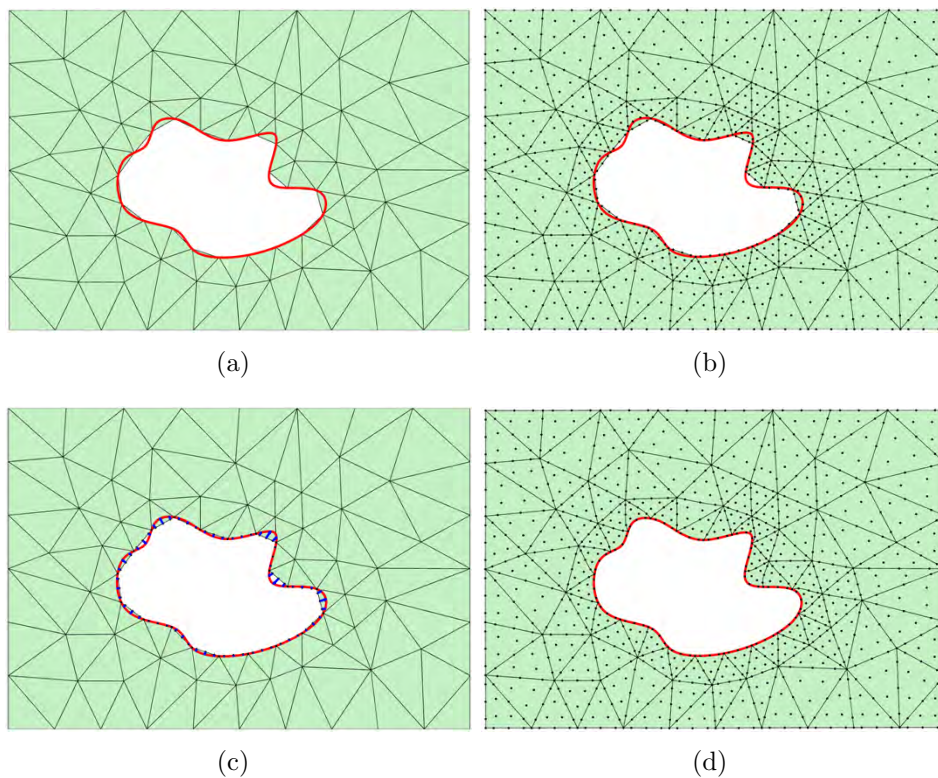


Figure 1: Illustration of steps involved in the proposed method for generating high-order curved triangular elements in two dimensions: (a) initial mesh with straight-sided elements; (b) high-order nodal distribution on the straight-sided elements; (c) imposed displacement at nodes on the curved portion of the boundary; (d) final curved high-order mesh.

3.1. Curved high-order edge nodal distribution

The key ingredient in ensuring that the process described results in a curved high quality mesh of high-order elements is the approach adopted to computing the desired location of the nodes on each curved boundary edge. The approach advocated here begins with a parameterisation of the true boundary of the computational domain in the form

$$\mathbf{C} : [0, 1] \longrightarrow \mathbf{C}([0, 1]) \subseteq \Gamma \subset \mathbb{R}^2$$

Standard choices for parameterising the boundary within a CAD system are polynomial B-splines, non-uniform rational B-splines (NURBS [21]) or subdivision surfaces [14]. Here, it is the NURBS boundary representation of the domain that is considered.

For an edge on a curved boundary, with vertices \mathbf{x}_1 and \mathbf{x}_{p+1} , the parametric coordinates λ_1 and λ_{p+1} of the two vertices are computed, from the parameterisation, as

$$\mathbf{C}(\lambda_i) = \mathbf{x}_i, \quad i = 1, p + 1$$

using a point inversion algorithm [21]. For a curve \mathbf{C} , parameterised by its arc length, a nodal distribution is specified in the parametric space between λ_1 and λ_{p+1} and this is mapped to the physical space using the parametrisation \mathbf{C} . This provides the desired nodal distribution over the true boundary, e.g. if a mesh with $p = 2$ is desired, the location of the mid edge node in the physical space is given by $\mathbf{C}((\lambda_1 + \lambda_3)/2)$. The nodal distribution is usually specified to be equally-spaced or to correspond to the location of the Fekete points.

Unfortunately, NURBS curves are rarely parameterised in terms of arc-length, so that obtaining the desired nodal distribution in the physical space is not trivial. The problem involves finding a nodal distribution in the parametric space which, when mapped with \mathbf{C} , corresponds to an equally-spaced or a Fekete-nodal distribution in the physical space. The length of the curved edge, defined by

$$L = \int_{\Gamma} d\mathbf{x} = \int_{\lambda_1}^{\lambda_{p+1}} |\mathbf{C}'(\lambda)| d\lambda$$

is evaluated approximately using a high-order Gauss-Legendre quadrature [23]. In practice, an adaptive quadrature is used, to ensure a relative error that is smaller than 10^{-4} , and composite quadratures are used to account for changes in the NURBS definition in $[\lambda_1, \lambda_{p+1}]$. Given a p -th degree nodal

distribution, $\{\xi\}_{k=1}^{p+1} \in [0, 1]$, the lengths of the subintervals $[\xi_k, \xi_{k+1}]$ are defined by

$$l_k = \xi_{k+1} - \xi_k \quad k = 1, \dots, p$$

The parametric coordinates, $\{\lambda_k\}_{k=2}^p$, of internal edge nodes are found by using a standard root finding algorithm to solve the set

$$\frac{1}{L} \int_{\lambda_1}^{\lambda_k} |\mathbf{C}'(\lambda)| d\lambda - \sum_{j=1}^{k-1} l_j = 0 \quad k = 2, \dots, p$$

of independent non-linear equations. This equation set is solved using a simple and robust bisection algorithm and, as it is possible to select a good initial guess, convergence is achieved in a few iterations. The NURBS parameterisation

$$\mathbf{x}_k = \mathbf{C}(\lambda_k), \quad k = 2, \dots, p \quad (4)$$

is employed to determine the position of the internal edge nodes in the physical space.

3.2. Two dimensional mesh

The high-order boundary nodal distribution, obtained by following the above procedure, is used to set the Dirichlet boundary conditions for the linear elastic problem. For each node on a curved boundary, the boundary condition imposes a displacement

$$\mathbf{u}_k = \mathbf{x}_k - \mathbf{x}_k^0$$

where \mathbf{x}_k^0 is the initial position of a boundary node and \mathbf{x}_k is the position given from equation (4).

The linear elastic problem described in Section 2 is solved and the result is a displacement field that, when applied to the original linear mesh, produces the desired high-order curved mesh.

4. Three dimensional curved mesh generation

The strategy adopted for generating curved high-order meshes in three dimensions is an extension of the process described for two dimensions. Initially, a linear mesh is generated and a high-order nodal distribution of the desired degree of approximation is then located within each element. For each face representing a curved boundary, a desired distribution for the nodes over the true boundary is generated and the linear elasticity problem is then solved to obtain the curved high-order mesh.

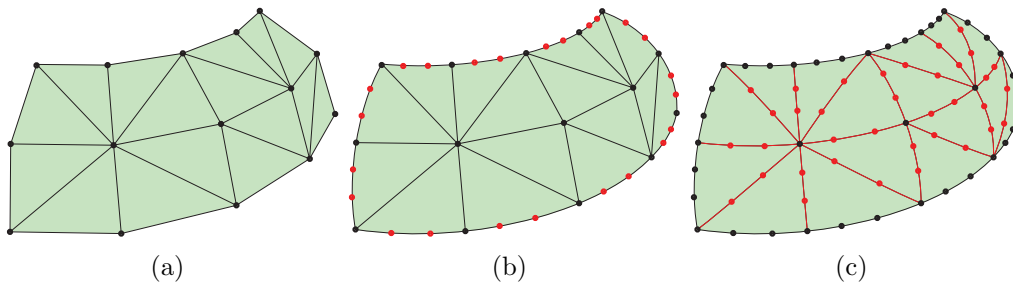


Figure 2: Illustration of the proposed high-order mesh generation for a surface patch: (a) the initial linear triangular surface mesh; (b) the high-order nodal distribution constructed on each edge of the patch boundary; (c) the high-order nodal distribution constructed on each internal edge.

4.1. Curved high-order edge nodal distribution

The initial linear triangular mesh used to represent a surface patch, making up a portion of a curved boundary, is illustrated in Figure 2 (a). Edges that lie on a curved boundary are classified into two categories: either edges that belong to a surface patch boundary or edges that are internal to a surface patch. In this case, a parameterisation of the form

$$\mathbf{S} : [0, 1]^2 \longrightarrow \mathcal{S}([0, 1]^2) \subseteq \Gamma \subset \mathbb{R}^3$$

is assumed for each curved boundary. For edges on the boundary of a surface patch, the desired nodal distribution is generated in the physical space, as shown in Figure 2 (b). Again, an equally-spaced distribution or the Fekete point location is normally employed. The procedure described above for generation of edge nodal distributions in two dimensions can be directly used, as the surface parameterisation is, when restricted to a patch boundary, just a parametric curve in three dimensions. In this example, an equally-spaced nodal distribution for a degree of approximation $p = 3$ has been selected. For an edge that does not lie on the boundary of a surface patch, the geodesic connecting the two edge vertices is approximated and the appropriate nodal distribution is generated in the physical space, as shown in Figure 2 (c).

The approximation of the geodesic connecting two edge vertices \mathbf{x}_1 and \mathbf{x}_2 is performed by iteratively constructing a list of points in the parametric space, such that the image of these points in the boundary surface parameterisation \mathbf{S} approximates the geodesic. As a first step, the parametric

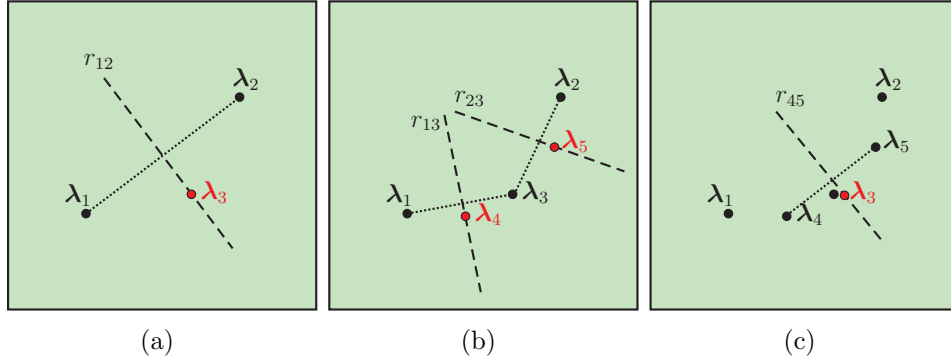


Figure 3: Illustration of the procedure for approximating the geodesic between two points in the parametric space: (a) selection of a point λ_3 on the perpendicular bisector between λ_1 and λ_2 such that equation (5) is satisfied; (b) selection of points λ_4 and λ_5 ; (c) correction of λ_3 using the perpendicular bisector to the segment joining λ_4 and λ_5 .

coordinates, λ_1 and λ_2 , of the edge vertices are found such that

$$\mathbf{S}(\lambda_i) = \mathbf{x}_i \quad i = 1, 2$$

Then, the point λ_3 in the parametric space is determined, such that it belongs to the perpendicular bisector of the segment connecting λ_1 and λ_2 , say r_{12} , and it satisfies

$$d(\mathbf{x}_1, \mathbf{S}(\lambda_3)) + d(\mathbf{S}(\lambda_3), \mathbf{x}_2) = \min_{\lambda \in r_{12}} \left\{ d(\mathbf{x}_1, \mathbf{S}(\lambda)) + d(\mathbf{S}(\lambda), \mathbf{x}_2) \right\} \quad (5)$$

Here, $d(\cdot, \cdot)$ denotes the Euclidean distance. This process is illustrated in Figure 3 (a). The point $\mathbf{x}_3 = \mathbf{S}(\lambda_3)$ is added to the list of points approximating the geodesic and the process is repeated between both \mathbf{x}_1 and \mathbf{x}_3 and between \mathbf{x}_3 and \mathbf{x}_2 , as shown in Figure 3 (b). The result is a point, λ_4 , on the perpendicular bisector of the line joining λ_1 and λ_3 and a point, λ_5 , on the perpendicular bisector of the line joining λ_3 and λ_2 . The position of λ_3 is corrected by using the perpendicular bisector of the line between λ_4 and λ_5 , as shown in Figure 3 (c). The process is repeated iteratively until a fine distribution of nodes that approximate, with a specified accuracy, the geodesic connecting \mathbf{x}_1 and \mathbf{x}_2 is obtained. A nodal distribution, of the desired degree of approximation p , can then be defined on the approximated geodesic.

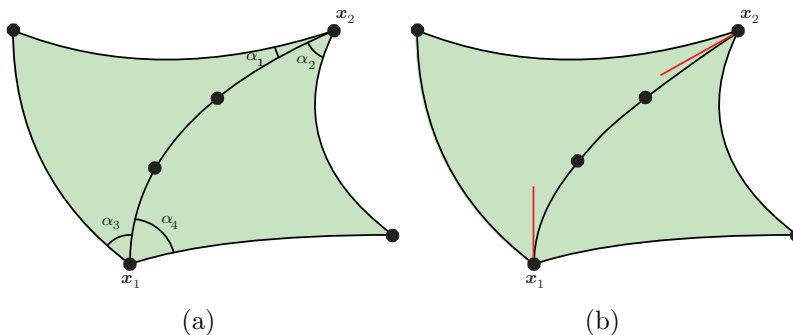


Figure 4: Two triangular faces on a curved boundary showing (a) a curved edge that forms an angle, α_1 , less than the specified limit; (b) correction of the edge for a cubic interpolation

Finally, the angle between neighboring edges is checked to ensure that the minimum angle is not less than a specified lower limit. For each edge on a curved boundary, e.g. the edge connecting vertices \mathbf{x}_1 and \mathbf{x}_2 in Figure 4 (a), the angles, α_i for $i = 1, \dots, 4$, between this edge and its neighboring edges are measured. If any angle α_i is less than the specified lower limit, a new edge connecting the vertices \mathbf{x}_1 and \mathbf{x}_2 is defined, in such a way that the four angles α_i for $i = 1, \dots, 4$ are acceptable. For instance, if a degree of approximation $p = 3$ is considered, the new edge is defined by a cubic curve, that contains the two vertices \mathbf{x}_1 and \mathbf{x}_2 , with the derivative at the initial and final vertices imposed in such a way that the minimum angle between edges is not less than the specified limit, as shown in Figure 4 (b). For a degree of approximation $p = 4$, the curvature on one edge vertex is also imposed and, for a degree of approximation $p = 5$, the curvature at both edge vertices is included. Extra conditions can be devised when using higher degrees of approximation, but these are not considered here.

4.2. Curved high-order surface mesh

A reference element, with a nodal distribution of the desired degree, is employed to generate the internal nodes on a curved boundary face. The reference element enables the computation of the distance from an internal node to the element boundaries. Using the geodesics in the physical space, internal points are placed on the curved faces by imposing the criterion that the relative distance, with respect to the element boundaries, is approximately

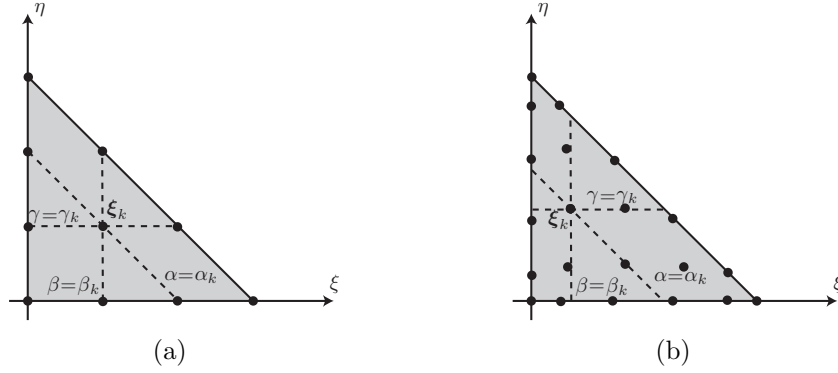


Figure 5: Reference triangle showing the barycentric coordinates of an internal point for (a) an equally-spaced nodal distribution for $p = 3$; (b) a Fekete-nodal distribution for $p = 5$

the same as that for the corresponding node in the reference element.

The procedure for placing high-order interior nodes for triangular faces is considered first. A p -th degree nodal distribution is defined on a reference element, e.g. Figures 5 (a) and (b) show an equally-spaced nodal distribution of degree $p = 3$ and a Fekete-nodal distribution of degree $p = 5$ respectively in the reference triangle. The barycentric coordinates, denoted by (α, β, γ) , for an internal node with local coordinates $\xi_k = (\xi_k, \eta_k)$, are given by $(\alpha_k, \beta_k, \gamma_k) = (1 - \xi_k - \eta_k, \xi_k, \eta_k)$, as illustrated in Figure 5. Note that the barycentric isolines intersect the boundary of the reference element at the location of the nodes, if the nodal distribution is equally-spaced, as shown in Figure 5 (a). However, this is not the case in general, as shown in Figure 5 (b) for the case of a Fekete nodal distribution.

The barycentric coordinates of an internal node can be used to define three geodesics, g^α , g^β and g^γ , in the physical space. The geodesic, g^α , joins the points \mathbf{x}_{12}^α and \mathbf{x}_{13}^α , where \mathbf{x}_{IJ}^α lies on the geodesic, g_{IJ} , connecting the vertices \mathbf{x}_I and \mathbf{x}_J . In this case,

$$d_{\mathcal{S}}(\mathbf{x}_I, \mathbf{x}_{IJ}^\alpha) = (1 - \alpha_k)d_{\mathcal{S}}(\mathbf{x}_I, \mathbf{x}_J)$$

where $d_{\mathcal{S}}$ denotes the distance function over the surface parametrised by \mathcal{S} , i.e. the distance along the geodesic between two points. Similarly, g^β joins the points \mathbf{x}_{21}^β and \mathbf{x}_{23}^β , where $\mathbf{x}_{IJ}^\beta \in g_{IJ}$ and

$$d_{\mathcal{S}}(\mathbf{x}_I, \mathbf{x}_{IJ}^\beta) = (1 - \beta_k)d_{\mathcal{S}}(\mathbf{x}_I, \mathbf{x}_J)$$

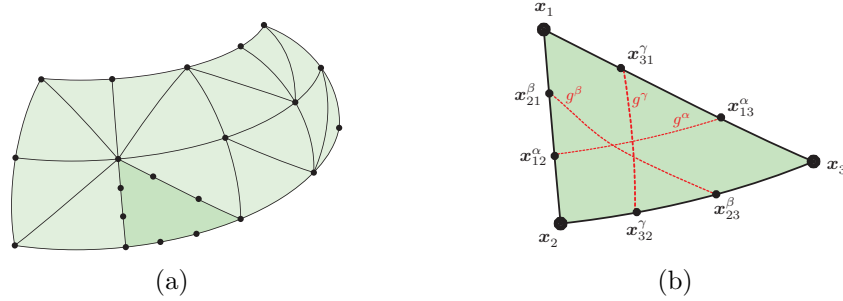


Figure 6: Surface patch showing (a) a curved face; (b) the three geodesics used to determine the position of the internal node.

and g^γ joins the points \mathbf{x}_{31}^γ and \mathbf{x}_{32}^γ , where $\mathbf{x}_{IJ}^\gamma \in g_{IJ}$ and

$$d_{\mathcal{S}}(\mathbf{x}_I, \mathbf{x}_{IJ}^\gamma) = (1 - \gamma_k) d_{\mathcal{S}}(\mathbf{x}_I, \mathbf{x}_J)$$

The three geodesics g^α , g^β and g^γ , corresponding to the internal node for an equally-spaced nodal distribution with $p = 3$, are illustrated in Figure 6.

The points $\mathbf{x}^\alpha \in g^\alpha$, $\mathbf{x}^\beta \in g^\beta$ and $\mathbf{x}^\gamma \in g^\gamma$ are defined such that

$$\begin{aligned} d_{\mathcal{S}}(\mathbf{x}_{12}^\alpha, \mathbf{x}^\alpha) &= \frac{\gamma_k}{\beta_k + \gamma_k} d_{\mathcal{S}}(\mathbf{x}_{12}^\alpha, \mathbf{x}_{23}^\alpha) \\ d_{\mathcal{S}}(\mathbf{x}_{21}^\beta, \mathbf{x}^\beta) &= \frac{\gamma_k}{\gamma_k + \alpha_k \sqrt{2}} d_{\mathcal{S}}(\mathbf{x}_{21}^\beta, \mathbf{x}_{23}^\beta) \\ d_{\mathcal{S}}(\mathbf{x}_{31}^\gamma, \mathbf{x}^\gamma) &= \frac{\beta_k}{\beta_k + \alpha_k \sqrt{2}} d_{\mathcal{S}}(\mathbf{x}_{31}^\gamma, \mathbf{x}_{32}^\gamma) \end{aligned}$$

and the position of the internal face node in the physical space is defined as the projection over the true surface of the average position of \mathbf{x}^α , \mathbf{x}^β and \mathbf{x}^γ , i.e.

$$\mathbf{x}_k = \Pi_{\mathcal{S}}\left(\frac{\mathbf{x}^\alpha + \mathbf{x}^\beta + \mathbf{x}^\gamma}{3}\right) \quad (6)$$

Here $\Pi_{\mathcal{S}}$ represents the projection operator over the surface parameterised by \mathcal{S} .

A similar procedure is adopted for curved quadrilateral faces, but now only two geodesics are considered, corresponding to the local coordinates of an internal node. Figure 7 shows a Fekete-nodal distribution for $p = 5$ in the reference square and the local coordinates of an internal node. The geodesic,

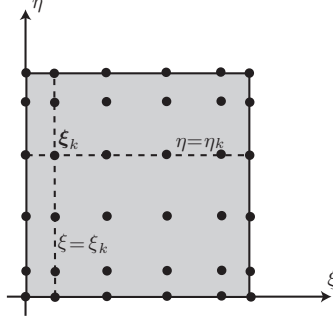


Figure 7: Reference square, with a Fekete-nodal distribution, for $p = 5$ and the local coordinates for an interior node

g^ξ , joins the points \mathbf{x}_{12}^ξ and \mathbf{x}_{43}^ξ , where $\mathbf{x}_{IJ}^\xi \in g_{IJ}$, and

$$d_{\mathcal{S}}(\mathbf{x}_I, \mathbf{x}_{IJ}^\xi) = (1 - \xi_k) d_{\mathcal{S}}(\mathbf{x}_I, \mathbf{x}_J)$$

Similarly, the geodesic g^η joins the points \mathbf{x}_{23}^η and \mathbf{x}_{14}^η , where $\mathbf{x}_{IJ}^\eta \in g_{IJ}$, and

$$d_{\mathcal{S}}(\mathbf{x}_I, \mathbf{x}_{IJ}^\eta) = (1 - \eta_k) d_{\mathcal{S}}(\mathbf{x}_I, \mathbf{x}_J)$$

It is worth noting, as shown in Figure 8, that the location of the points \mathbf{x}_{IJ}^ξ and \mathbf{x}_{IJ}^η coincides with high-order edge nodes computed in Section 4.1, as the nodal distribution in the reference square is a tensor product of one dimensional nodal distributions. The points $\mathbf{x}^\xi \in g^\xi$ and $\mathbf{x}^\eta \in g^\eta$ are defined such that

$$\begin{aligned} d_{\mathcal{S}}(\mathbf{x}_{12}^\xi, \mathbf{x}^\xi) &= \xi_k d_{\mathcal{S}}(\mathbf{x}_{12}^\xi, \mathbf{x}_{43}^\xi) \\ d_{\mathcal{S}}(\mathbf{x}_{14}^\eta, \mathbf{x}^\eta) &= \eta_k d_{\mathcal{S}}(\mathbf{x}_{14}^\eta, \mathbf{x}_{23}^\eta) \end{aligned}$$

and the position of the internal face node in the physical space is defined as

$$\mathbf{x}_k = \Pi_{\mathcal{S}}\left(\frac{\mathbf{x}^\xi + \mathbf{x}^\eta}{2}\right) \quad (7)$$

which is the projection over the true surface of the average position of \mathbf{x}^ξ and \mathbf{x}^η .

4.3. Three dimensional mesh

The resulting high-order boundary nodal distribution is used to set the Dirichlet boundary conditions for the linear elastic problem. For each node

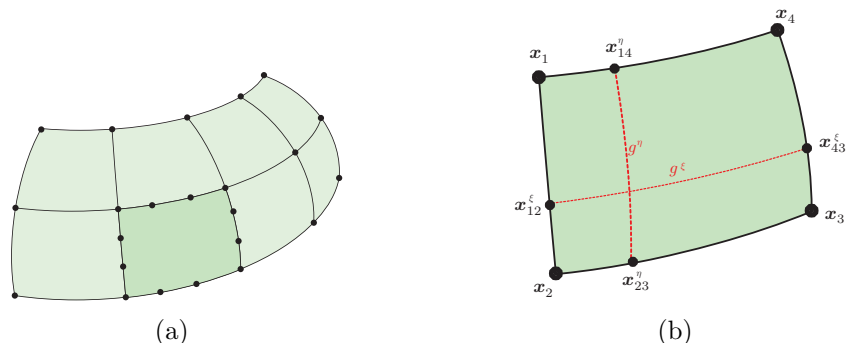


Figure 8: Surface patch showing (a) a curved quadrilateral face; (b) the two geodesics used to determine the position of the internal node.

on a curved boundary, the boundary condition imposes a displacement of the form

$$\mathbf{u}_k = \mathbf{x}_k - \mathbf{x}_k^0$$

where \mathbf{x}_k^0 is the initial position of a boundary node and \mathbf{x}_k is the position given by equation (6), for a curved triangular face, or by equation (7), for a curved quadrilateral face. The linear elastic problem described in Section 2 is solved and the result is a displacement field that, when applied to the original mesh, produces the desired high-order curved mesh. For realistic three dimensional viscous flow problems, the linear system of equations may contain millions of unknowns. In this case it is preferable to split the system into a number of smaller problems. For example, boundary layer meshes are normally generated using a layer by layer strategy, so that the system corresponding to the first layer of elements surrounding the aerodynamic shape can be solved, using Dirichlet boundary conditions on the curved boundary and a homogeneous Neumann boundary condition on the outer surface of the layer. The system corresponding to the second layer of elements can then be solved, using the displacement field from the outer boundary of the first layer as a Dirichlet boundary condition. The procedure continues until the last layer of elements is deformed or until the displacement field of one layer is small enough. It is worth recalling that, in case of tetrahedral meshes, the presence of a large number of elements with planar faces leads to an extra efficiency of the finite element solver. This is because the mapping between the reference element and the physical elements is then an affine mapping,

i.e. the determinant of the Jacobian of the isoparametric transformation is constant. The layer by layer approach means that the deformation process can be stopped when a quality measure has not substantially changed after applying the deformation. For the generation of the anisotropic meshes shown in Section 5, the layer by layer approach is implemented.

When we have very large meshes, with refined layers of elements near solid surfaces, we can use the Solid–Extension–Mesh Moving Technique (SEMMT) [31], particularly its multi-domain version (SEMMT-MD), to efficiently solve the mesh moving equations. This would result in a robust way of solving the mesh movement equations iteratively, even with stretched elements near solid surfaces.

Although other measures of the element quality can be considered [22], the scaled Jacobian [6] is employed here as a measure of the distortion of a curved high–order isoparametric finite element. This is defined as

$$\hat{I} = \frac{\min_{\boldsymbol{\xi} \in R} |\mathbf{J}(\boldsymbol{\xi})|}{\max_{\boldsymbol{\xi} \in R} |\mathbf{J}(\boldsymbol{\xi})|} \quad (8)$$

where

$$\mathbf{J}(\boldsymbol{\xi}) = \frac{\partial \mathbf{x}(\boldsymbol{\xi})}{\partial \boldsymbol{\xi}}$$

is the Jacobian of the isoparametric mapping of equation (3). To ensure that the curved high–order mesh is valid, it is necessary to verify that

$$|\mathbf{J}(\boldsymbol{\xi})| > 0 \quad \forall \boldsymbol{\xi} \in e$$

for all the elements in the mesh. In practice, the determinant of the Jacobian $|\mathbf{J}(\boldsymbol{\xi})|$ is actually checked at a set of discrete points [6] in the reference element e . The points used are chosen to be those corresponding to a quadrature rule of order $2p$ for a curved high–order element of degree p , i.e. the quadrature points necessary to integrate exactly the element mass matrix with an approximation of degree p . This check does not remove completely the possibility that the mesh may contain elements with a negative Jacobian [12]. With the standard definition of the scaled Jacobian given in equation (8), it is possible to obtain a positive scaled Jacobian even when the element is not valid, e.g. if the Jacobian is negative at all the selected points. For this reason, the slightly modified definition

$$I = \frac{\min_{\boldsymbol{\xi} \in R} |\mathbf{J}(\boldsymbol{\xi})|}{|\max_{\boldsymbol{\xi} \in R} |\mathbf{J}(\boldsymbol{\xi})||}$$

is employed as the indicator of the validity of an element. With this revised definition, a negative value indicates that the element is not valid, a positive value indicates that the element is valid and the classical distortion measure is recovered, i.e. $I = \widehat{I}$.

5. Implementation Examples

Several examples, in both two and three dimensions, are considered to illustrate the potential of the proposed methodology. The examples that have been selected are of particular interest to the aerospace community, as they involve isotropic and anisotropic high-order curved meshes suitable for the computation of external flows around aerodynamic shapes.

The elastic parameter values $E = 10$ and $\nu = 0.4$ are used for all the examples. It has been found that this combination allows the minimum scaled Jacobian to be maximised and, at the same time, allows the condition number of the linear system to be minimised. The scaled Jacobian is found to be independent of the value of E and highly dependent on ν . Since the scaled Jacobian is a measure of the volumetric deformation, it is expected that, with lower values of ν , compressibility of the material will result in highly distorted elements near curved boundaries. The best element quality is expected for values of ν approaching the incompressible limit, as the imposed boundary displacement then propagates into the computational domain. This behaviour is confirmed in Figure 9 (a), which illustrates the influence of the elastic parameters on the scaled Jacobian. Figure 9 (b) shows that the condition number of the system matrix deteriorates rapidly as the value of E is increased. Values of ν between 0 and 0.4 are found to have little effect. For higher values of ν , i.e when the material approaches the incompressible limit, the effect is more pronounced and the condition number of the system matrix also deteriorates. Note that the exact nature of the plots shown in Figure 9 will depend upon the geometry under consideration. However, it is important to note that the same qualitative behavior has been consistently observed in practice for a number of different geometries.

5.1. Isotropic mesh for a NACA0012 aerofoil

The first example is the problem of generating an isotropic mesh, for a degree of approximation $p = 5$, in the region surrounding a NACA0012 aerofoil. Figures 10 (a) and (b) show an initial mesh of linear elements and the final high-order curved mesh respectively. A detail of the mesh in the

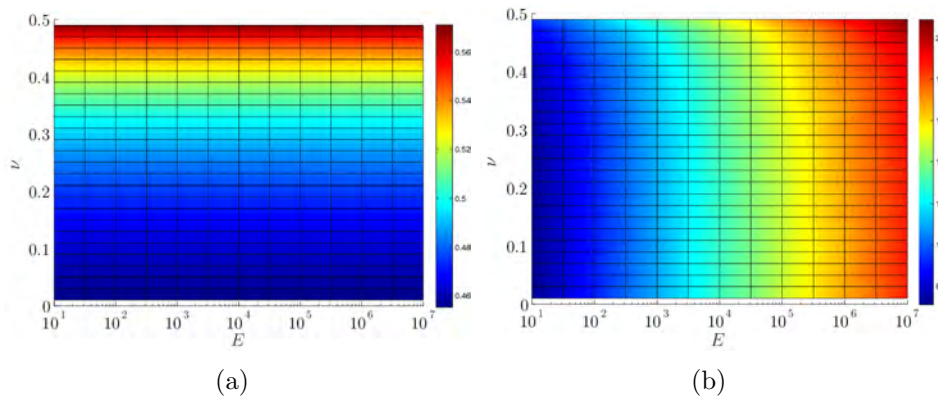


Figure 9: Influence of the elastic material parameters on (a) the scaled Jacobian; (b) the logarithm of the condition number of the system matrix.

vicinity of the leading edge of the aerofoil is shown in Figure 10 (c). This detail shows some of the curved elements and the high-order Fekete-nodal distribution on each element. The mesh has 370 vertices, 650 elements and 50 edges on the curved boundary. After introducing a high-order nodal distribution, appropriate for an approximation of degree $p = 5$ over each element, the resulting high-order mesh has 8 350 nodes. An example of a high-order curved quadrilateral mesh generated for this configuration is given in Figure 11.

Figure 12 (a) displays a histogram of the scaled Jacobian, I , for the high-order triangular mesh. It shows the percentage of elements for a given scaled Jacobian in intervals of 0.05. For this simple isotropic case, 99% of the elements are such that $I > 0.95$ and the minimum value of the scaled Jacobian is 0.83.

To illustrate the optimal properties of meshes generated in this fashion, the interpolation error estimate for a smooth function is checked, on a series of curved triangular and quadrilateral high-order meshes with degree ranging from $p = 1$ up to $p = 7$. In order to measure the interpolation error, the nodal values of the solution are set by using the smooth function $f(x, y) = x \cos(y) + y \sin(x)$. Then, the error between the approximated solution, interpolated from the nodal values, and the exact solution is computed at each quadrature point in order to compute the $\mathcal{L}^2(\Omega)$ error. Figure 12 (b) shows the evolution of this error, as a function of the square root of the

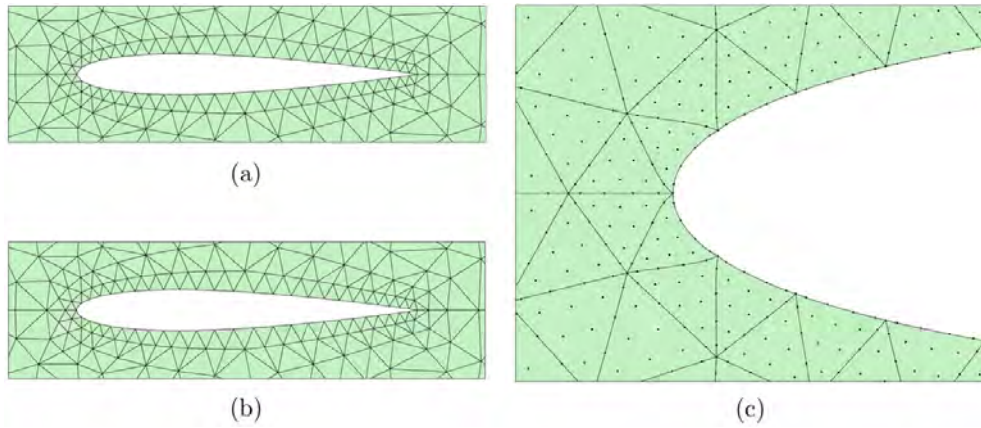


Figure 10: NACA0012 aerofoil showing (a) an initial mesh with straight-sided triangular elements; (b) a curved high-order mesh; (c) a detail of the curved mesh near the leading edge with a high-order Fekete-nodal distribution on each element.

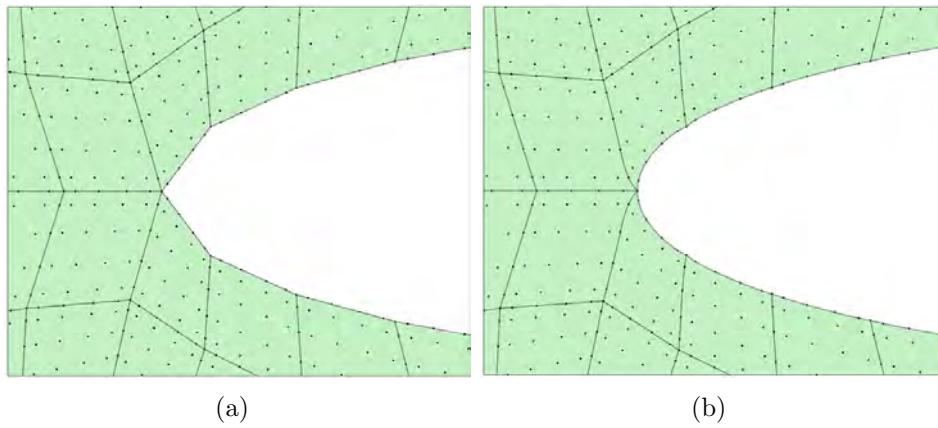


Figure 11: NACA0012 aerofoil: detail near the leading edge showing (a) the initial mesh with straight-sided quadrilateral elements and (b) the curved high-order mesh

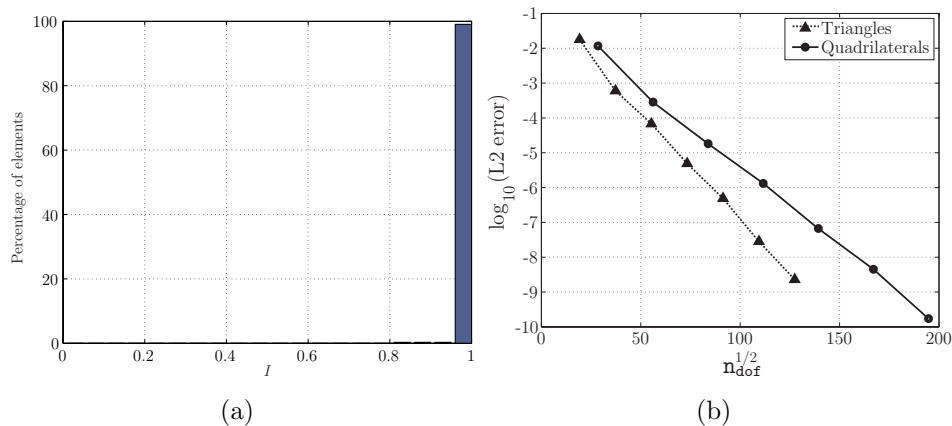


Figure 12: NACA0012 aerofoil showing (a) the scaled Jacobian; (b) an illustration of the optimality of the mesh for finite element analysis.

number of degrees of freedom n_{dof} , on both the triangular and quadrilateral elements. The exponential convergence that is expected in the approximation of a smooth function is observed, demonstrating that the proposed strategy produces optimal meshes for finite element analysis.

5.2. Isotropic mesh for a generic Falcon aircraft

This example indicates the use of the approach for the generation of an isotropic mesh in the region surrounding a complex aircraft configuration. Figure 13 shows a view of the high-order surface mesh produced after applying the proposed approach. A detail of a view of the high-order surface mesh and the nodal distribution, for use with a degree of approximation $p = 3$, near the engine intake is shown in Figure 14 (a). A detail of a cut through the mesh, in the vicinity of the aircraft surface, is shown in Figure 14 (b). The mesh has 27 842 vertices, 150 801 elements and 3 686 triangular faces on the aircraft. For a degree of approximation $p = 3$, the total number of nodes in this mesh is 703 938.

An indication of the distribution of the values of the scaled Jacobian for this mesh is shown in the histogram of Figure 15. For this complex geometry, the proposed approach produces a high-order mesh in which almost 97% of the elements have a scaled Jacobian value $I > 0.95$. However, it should be noted that the minimum value of I is now significantly smaller than that produced in the previous two dimensional examples. For this mesh, there are two elements which are such that $0.15 < I < 0.2$ and 75 elements for

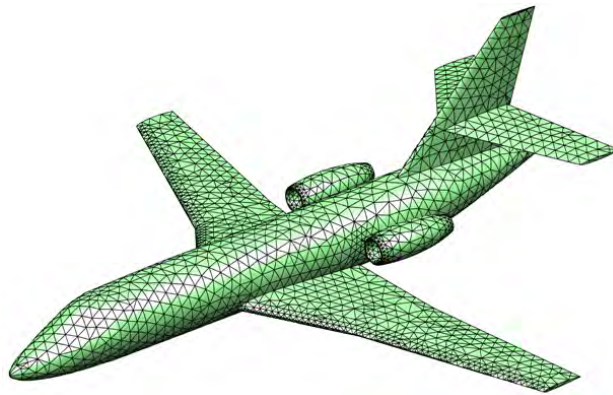


Figure 13: Isotropic curved high-order surface mesh for a generic Falcon aircraft.

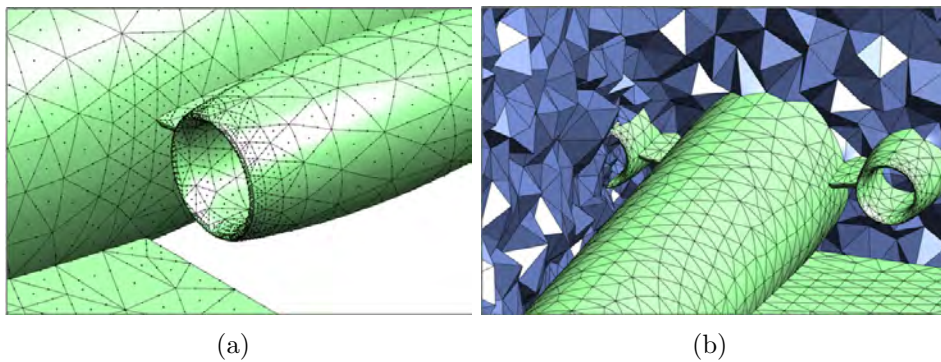


Figure 14: Isotropic mesh for a Falcon aircraft showing (a) a detail of a view of the surface mesh with the nodal distribution near the engine intake; (b) a detail of a cut through the interior volume mesh.

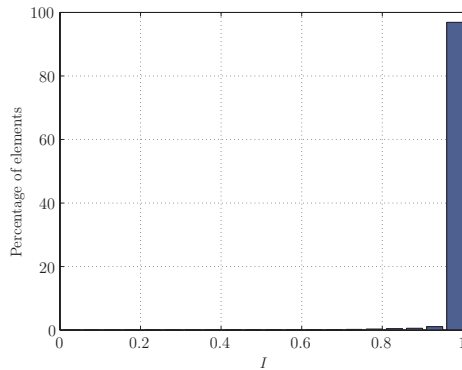


Figure 15: Scaled Jacobian for the generic Falcon isotropic mesh

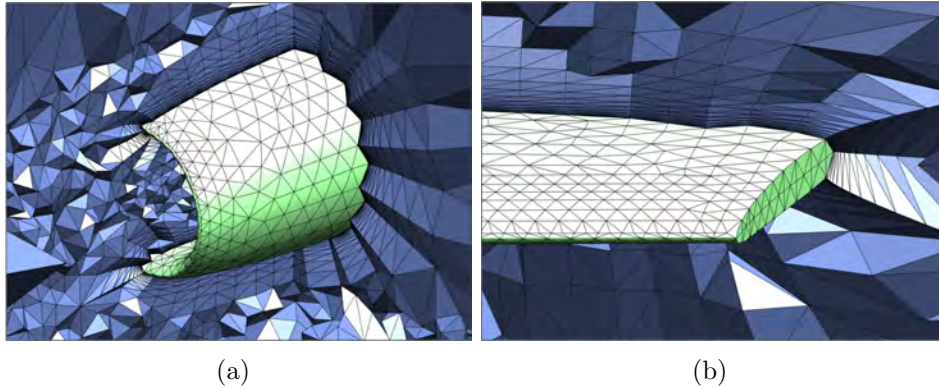


Figure 16: Anisotropic mesh for a generic Falcon aircraft showing the form of the mesh (a) near the engine intake; (b) near the wing tip.

which $I < 0.5$. As might be expected, these elements are located in critical regions of the mesh, such as the leading edge of the wings and the engine intake. The low quality of these elements can be mainly attributed to the low resolution provided by the cubic approximation when attempting to capture the large deformations in regions with high curvature. It is worth recalling that, although the linear elastic model has been selected for its efficiency, cases such as this can violate the small deformation hypothesis inherent in the linear model. Refining the initial linear mesh, or increasing the degree of the approximation employed, may alleviate this problem, especially in the vicinity of regions with high curvature.

5.3. Anisotropic mesh for a generic Falcon aircraft

A more complex example is the problem of generating an anisotropic mesh for analysing viscous flow over a generic Falcon aircraft configuration. Details of cuts through the mesh, shown in Figures 16 (a) and (b), illustrate the form of the boundary layer mesh in the difficult regions near the engine intake and the wing tip respectively.

The mesh has 228 845 vertices, 1 303 733 elements and 24 670 triangular faces on the aircraft surface. For a degree of approximation $p = 3$, the total number of nodes in this mesh is 5 967 338. An indication of the amount of element stretching in the mesh is represented in the histogram of Figure 17 (a). The maximum stretching is almost 381 and there are over 300 elements have a stretching of more than 200. The histogram of the scaled Jacobian for the

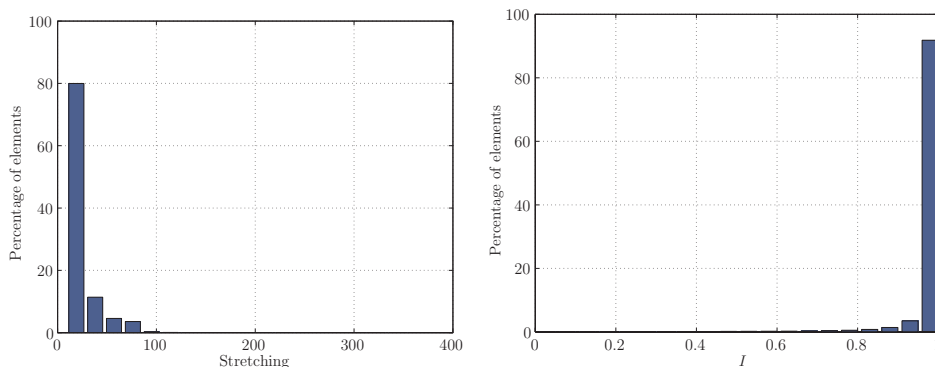


Figure 17: Anisotropic mesh for a generic Falcon aircraft showing (a) the stretching; (b) the scaled Jacobian.

elements in the mesh are shown in Figure 17 (b). For this complex configuration, more than 91% of the elements have a scaled Jacobian value $I > 0.95$. However, the minimum value of I is now 0.08 and 6 938 elements are such that $I < 0.5$.

5.4. Anisotropic mesh for the F6 configuration

The final example involves the generation of an anisotropic mesh suitable for analysing viscous flow over the F6 aircraft configuration introduced in the 2nd AIAA CFD Drag Prediction Workshop [2]. A detail of a view of the surface mesh is given in Figure 18, showing the important regions near the engine intake and at the leading edge of the wing. Views of cuts through the volume mesh, near the engine intake and near the leading edge of the wing, are given in Figure 19. The mesh has 803 345 vertices, 4 624 321 elements and 79 052 triangular faces on the aircraft surface. For a degree of approximation $p = 3$, the total number of nodes in this mesh is 21 113 641.

Figure 20 (a) gives information on the amount of element stretching. The maximum stretching is 320 and there are more than 5 000 elements with a stretching of more than 200. The histogram of the scaled Jacobian values is shown in Figure 20 (b). For this complex anisotropic mesh, more than 95% of the elements have a scaled Jacobian value $I > 0.95$. The minimum value of I for this mesh is 0.015 and 15 030 elements have a value of I which is less than 0.5.

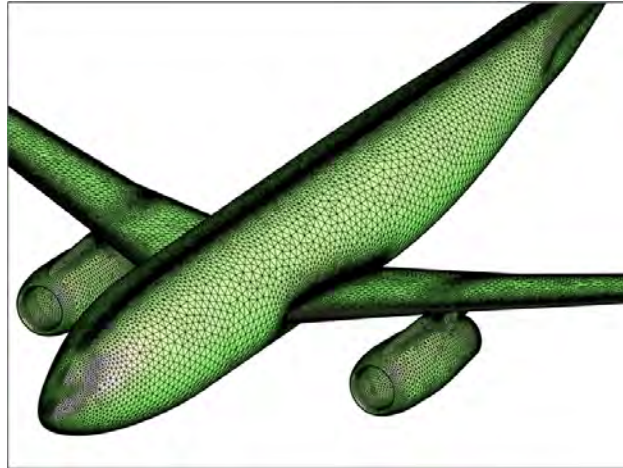


Figure 18: Anisotropic mesh generation for the F6 configuration showing a detail of the surface mesh near the engine intake and the leading edge of the wing.

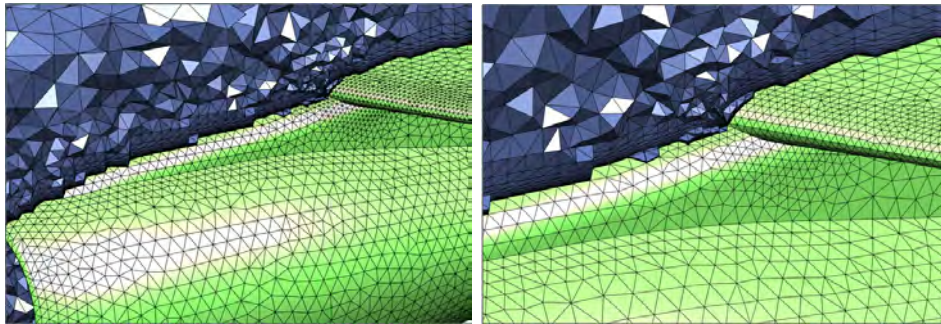


Figure 19: Anisotropic mesh generation for the F6 configuration showing views of a cut through the volume mesh near the engine intake and near the leading edge of the wing.

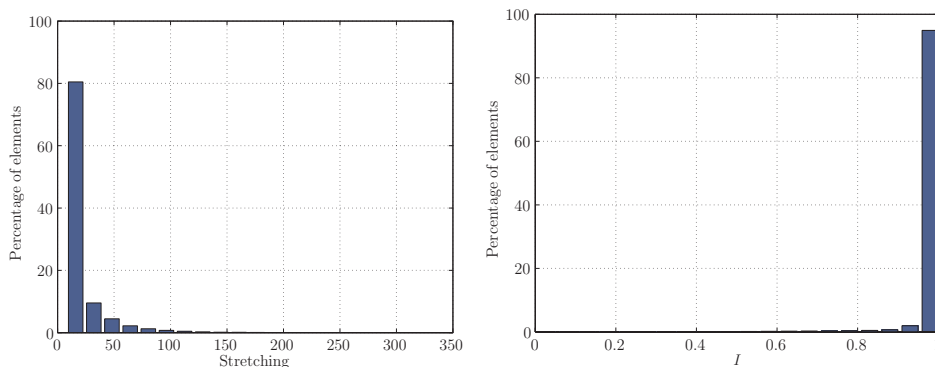


Figure 20: F6 configuration: (a) stretching and (b) scaled Jacobian

6. Conclusions

An *a posteriori* strategy for obtaining high-order curved meshes, suitable for finite element analysis in both two and three dimensions, has been described. The method is based on deforming an initial mesh with planar faces and edges using a linear elasticity model. The proposed methodology is valid for any element topology and hybrid meshes, containing different types of element, can be handled. Special attention has been paid to the construction of high-order nodal distributions on edges and faces on curved boundaries. The quality of the resulting meshes was analysed in terms of the scaled Jacobian, which is a standard distortion measure for curved elements.

Several examples, involving geometries of complex shape in both two and three dimensions, have been considered to demonstrate the potential of the proposed methodology. Special emphasis has been placed on constructing high-order curved meshes for geometries that are of particular interest to the aerospace community. In this area, anisotropic meshes suitable for analysing viscous flow over two complex aircraft configurations have been presented.

References

- [1] Bassi, F., Rebay, S.: High-order accurate discontinuous finite element solution of the 2D Euler equations. *J. Comput. Phys.* **138**(2), 251–285 (1997)
- [2] Brodersen, O., Stürmer, A.: Drag prediction of engine–airframe inter-

- ference effects using unstructured Navier–Stokes calculations. In: 19th AIAA Applied Aerodynamics Conference. AIAA (2001)
- [3] Chen, Q., Babuška, I.: Approximate optimal points for polynomial interpolation of real functions in an interval and in a triangle. *Comput. Methods Appl. Mech. Eng.* **128**(3–4), 405–417 (1995)
 - [4] Chen, Q., Babuška, I.: The optimal symmetrical points for polynomial interpolation of real functions in the tetrahedron. *Comput. Methods Appl. Mech. Eng.* **137**(1), 89–94 (1996)
 - [5] Davies, R.W., Morgan, K., Hassan, O.: A high order hybrid finite element method applied to the solution of electromagnetic wave scattering problems in the time domain. *Comput. Mech.* **44**(3), 321–331 (2009)
 - [6] Dey, S., O’Bara, R.M., Shephard, M.S.: Curvilinear mesh generation in 3D. In: 8th International Meshing Roundtable. Sandia National Laboratories (1999)
 - [7] Dey, S., O’Bara, R.M., Shephard, M.S.: Towards curvilinear meshing in 3D: the case of quadratic simplices. *Computer-Aided Design* **33**(3), 199 – 209 (2001)
 - [8] Dey, S., Shephard, M.S., Flaherty, J.E.: Geometry representation issues associated with p -version finite element computations. *Comput. Methods Appl. Mech. Engrg.* **150**(1-4), 39–55 (1997)
 - [9] Dunavant, D.A.: High degree efficient symmetrical gaussian quadrature rules for the triangle. *International Journal for Numerical Methods in Engineering* **21**(6), 1129–1148 (1985)
 - [10] Felippa, C.A.: A compendium of FEM integration formulas for symbolic work. *Engineering Computations* **21**(8), 867–890 (2004)
 - [11] Hesthaven, J.S., Warburton, T.: *Nodal Discontinuous Galerkin Methods: Algorithms, Analysis, and Applications*, vol. 54. Springer Verlag (2008)
 - [12] Johnen, A., Remacle, J.F., Geuzaine, C.: Geometrical validity of curvilinear finite elements. In: 20th International Meshing Roundtable, pp. 255–271. Sandia National Laboratories (2011)

- [13] Johnson, A.A., Tezduyar, T.E.: Mesh update strategies in parallel finite element computations of flow problems with moving boundaries and interfaces. *Comput. Methods Appl. Mech. Eng.* **119**(1–2), 73–94 (1994)
- [14] Jörg, P., Ulrich, R.: Subdivision Surfaces, *Geometry and Computing*, vol. 3. Springer-Verlag, Berlin (2008)
- [15] Karniadakis, G.E., Sherwin, S.J.: Spectral/*hp* element methods for computational fluid dynamics, 2nd. edn. Oxford University Press (2004)
- [16] Kroll, N.: The ADIGMA project. In: N. Kroll, H. Bieler, H. Deconinck, V. Couaillier, H. van der Ven, K. Sørensen (eds.) ADIGMA – A European initiative on the development of adaptive higher-order variational methods for aerospace applications, *Notes on Numerical Fluid Mechanics and Multidisciplinary Design*, vol. 113, chap. 1, pp. 1–9. Springer (2010)
- [17] Ledger, P.D., Morgan, K., Hassan, O.: Frequency and time domain electromagnetic scattering simulations employing higher order edge elements. *Comput. Methods Appl. Mech. Engrg.* **194**(2-5), 105–125 (2005)
- [18] Luo, X.J., Shephard, M.S., Remacle, J.F.: The influence of geometric approximation on the accuracy of higher order methods. In: 8th International Conference on Numerical Grid Generation in Computational Field Simulations (2002)
- [19] Luo, X.J., Shephard, M.S., Remacle, J.F., O’Bara, R.M., Beall, M.W., Szabó, B., Actis, R.: *p*-version mesh generation issues. In: 11th International Meshing Roundtable, pp. 343–354. Sandia National Laboratories (2002)
- [20] Persson, P.O., Peraire, J.: Curved mesh generation and mesh refinement using lagrangian solid mechanics. In: Proceedings of the 47th AIAA Aerospace Sciences Meeting and Exhibit. AIAA (2009)
- [21] Piegl, L., Tiller, W.: The NURBS Book. Springer-Verlag, London (1995)
- [22] Roca, X., Gargallo-Peiró, A., Sarrate, J.: Defining quality measures for high-order planar triangles and curved mesh generation. In: 20th International Meshing Roundtable, pp. 365–383. Sandia National Laboratories (2011)

- [23] Sevilla, R., Fernández-Méndez, S.: Numerical integration over 2D NURBS shaped domains with applications to NURBS-enhanced FEM. *Finite Elem. Anal. Des.* **47**(10), 1209–1220 (2011)
- [24] Sevilla, R., Fernández-Méndez, S., Huerta, A.: NURBS-enhanced finite element method (NEFEM). *Internat. J. Numer. Methods Engrg.* **76**(1), 56–83 (2008)
- [25] Sevilla, R., Fernández-Méndez, S., Huerta, A.: NURBS-enhanced finite element method (NEFEM) for Euler equations. *Internat. J. Numer. Methods Fluids* **57**(9), 1051–1069 (2008)
- [26] Sevilla, R., Fernández-Méndez, S., Huerta, A.: 3D NURBS-enhanced finite element method (NEFEM). *Internat. J. Numer. Methods Engrg.* **88**(2), 103–125 (2011)
- [27] Sevilla, R., Fernández-Méndez, S., Huerta, A.: Comparison of high-order curved finite elements. *Internat. J. Numer. Methods Engrg.* **87**(8), 719–734 (2011)
- [28] Sherwin, S.J., Peiró, J.: Mesh generation in curvilinear domains using high-order elements. *Internat. J. Numer. Methods Engrg.* **53**(1), 207–223 (2002)
- [29] Solin, P., Segeth, K.: *Higher-Order Finite Element Methods*. Chapman & Hall (2003)
- [30] Stein, K., Tezduyar, T.E., Benney, R.: Mesh moving techniques for fluid-structure interactions with large displacements. *J. Appl. Mech.* **70**(1), 58–63 (2003)
- [31] Stein, K., Tezduyar, T.E., Benney, R.: Automatic mesh update with the solid-extension mesh moving technique. *Comput. Methods Appl. Mech. Engrg.* **193**(21–22), 2019–2032 (2004)
- [32] Taylor, M.A., Wingate, B.A., Vincent, R.E.: An algorithm for computing Fekete points in the triangle. *SIAM J. Numer. Anal.* **38**(5), 1707–1720 (2000)
- [33] Tezduyar, T., Aliabadi, S., Behr, M., Johnson, A., Mittal, S.: Parallel finite-element computation of 3D flows. *Computer* **26**(10), 27–36 (1993)

- [34] Vincent, P.E., Jameson, A.: Facilitating the adoption of unstructured high-order methods amongst a wider community of fluid dynamicists. *Math. Model. Nat. Phenom.* **6**(3), 97–140 (2011)
- [35] Wandzura, S., Xiao, H.: Symmetric quadrature rules on a triangle. *Comput. Math. Appl.* **45**(12), 1829–1840 (2003)
- [36] Weatherill, N.P., Hassan, O.: Efficient three-dimensional Delaunay triangulation with automatic point creation and imposed boundary constraints. *Internat. J. Numer. Methods Engrg.* **37**(12), 2005–2039 (1994)
- [37] Xue, D., Demkowicz, L.: Control of geometry induced error in *hp* finite element (FE) simulations. I. Evaluation of FE error for curvilinear geometries. *Internat. J. Numer. Anal. Model.* **2**(3), 283–300 (2005)
- [38] Zienkiewicz, O.C., Morgan, K.: *Finite elements and approximation.* John Wiley & Sons (1983)
- [39] Zienkiewicz, O.C., Taylor, R.L.: *The Finite Element Method, vol. 1. The basis, fifth edn.* Butterworth-Heinemann (2000)